

The Application of the Fundamental Parameters Approach as Implemented in TOPAS to Divergent Beam Powder Diffraction Data

James P. Cline^a, David Black, David Gil, Albert Henins & Donald Windover

National Institute of Standards and Technology

Gaithersburg MD,

^ajcline@nist.gov

Keywords: Powder Diffraction, Fundamental Parameters Approach, Profile Fitting, Rietveld Analysis, Standard Reference Materials, Lattice Parameter Measurement

Abstract. The fundamental parameters approach (FPA) as implemented in TOPAS is investigated for analyses of conventional X-ray powder diffraction (XRPD) data. The FPA involves the convolution of a series of models, each one constituting an individual contribution to the geometric portion of the instrument profile function (IPF). Parameters within each model are refined by least squares to yield a presumably accurate description of the experiment. If one wishes to interrogate the functionality of said models, a diffractometer wherein the uncertainties in optical character are minimized is required. To this end, a diffractometer was built at NIST which featured conventional divergent beam optics in conjunction with a well aligned, stiff, and accurate goniometer assembly. Initial results indicated that the detector arm was flexing; this problem has been addressed with the fabrication and installation of a new arm and counterweight assembly. Data collected from NIST Standard Reference Material (SRM) 660a, lanthanum hexaboride, are analyzed using the FPA method to yield conclusions on the validity of the models with respect to shape and position of the diffraction profiles.

Introduction

The observed line shape in powder diffraction is known to consist of a convolution of contributions from the instrument, referred to as the geometric profile, the emission spectrum, and the sample, shown diagrammatically for divergent beam XRPD in Figure 1. The factors comprising the geometric profile are delineated in Table 1. It is primarily the geometric contribution to the observed profiles that leads to the well known complexity of X-ray line shapes from conventional XRPD equipment. Use of analytical profile fitting with profile shape functions such as Gaussian, Lorentzian, Voigt and pseudo-Voigt that vary as a function of 2θ have given credible results for a typical Rietveld [1,2] structure refinement. However, the quality of the fits, as reflected in the residual error terms, is invariably worse for conventional XRPD than other diffraction methods due to the aforementioned complexity in profile shape. Convolution-based profile fitting was proposed in 1954 [3] and much of the formalism of the aberration functions shown in Table 1 was developed by Wilson in 1963 [4]. However, limitations in computing capability largely prevented the realization of the full FPA method until 1992 with the work of Cheary and Coelho [5]. This was made available to the community through the program Xfit, later via KoalaRiet [6] and recently via TOPAS¹ [7]. The primary interest for this author in the FPA method is specific to measurements pertaining to SRM certification. The various aberrations affecting the diffraction line shape are such that the apparent profile maxima or centroids do not necessarily correspond to the d-spacing of the diffracting hkl plane except perhaps in a limited region of 2θ , emphasizing the need for accurate modeling of the observed line shape. The FPA method models the contributions to the observed

¹Certain commercial equipment, instruments, or materials are identified in this manuscript in order to adequately specify the experimental procedure. Such identification does not imply recommendation or endorsement by the National Institute of Standards and Technology, nor does it imply that the materials or equipment identified are necessarily the best available for the purpose.

profile in a physically interpretable manner. The parameter estimates resulting from the fitting may be checked for plausibility using physical first principles.

The wavelength profile, or emission spectrum illustrated in Figure 1 provides the traceability of the diffraction measurement to the SI [8]. The presently accepted characterization of the emission spectrum of Cu $K\alpha$ radiation is provided by Hölzer, *et al.* [9] and is shown in Figure 2. The spectrum is modeled with four Lorentzians; two large ones for the primary $K\alpha_1$ and $K\alpha_2$ profiles, and two smaller ones displaced slightly to larger wavelengths to account for the asymmetry in the observed line shape. At a slightly smaller wavelength than the $K\alpha_1$ are a series of weak ($\approx 1\%$), satellite lines [10], sometimes referred as the " $K\alpha_3$ " lines, which are modeled with a single Lorentzian. The data shown in Figure 2 are in wavelength space and are transformed into 2θ space with the dispersion relation. This is obtained by differentiating Bragg's law to obtain $d\theta/d\lambda$. The dominant term in the result is $\tan\theta$ which leads to the well known "stretching" of the wavelength distribution with respect to 2θ . Lastly are the "tube tails" reported by Bergmann, *et al.* [11]. This contribution is not technically related to the Cu emission spectrum, but is rather an artifact of the production of X-rays in a laboratory diffractometer. They arise from the off axis electrons accelerated into the tube anode that produce X-rays which originate from positions on the anode other than the expected line source. They are not within the expected trajectory of para-focusing X-ray optics and produce "tails" on either side of a line profile as illustrated in Figure 3.

X-Ray Diffractometer Construction and Alignment

We sought to evaluate the capability of the FPA for application to standard divergent beam X-ray optics. In order to test the models of the FPA, data are required which are not polluted by spurious aberrations not listed in Table 1. Rigorous analyses of data from Bragg-Brentano geometry require knowledge of both the diffraction angle and the effective source-sample-detector distances. Therefore a goniometer assembly is required that is not only capable of accurate angle measurement, but that is dimensionally stable and aligned with respect to its rotation axes to within $\approx 5\ \mu\text{m}$ for rotation center offset, and $\approx 0.0014^\circ$ (5 arc-seconds) for parallelism. Alignment of the X-ray optics must also be superlative in nature. To this end a diffractometer, the Ceramics Division Divergent Beam Diffractometer (CDDBD), shown in Figure 4, was built at NIST. An overhead cutaway schematic is shown in Figure 5. The goniometer assembly, of θ - 2θ geometry, includes of a pair of Huber 420 rotation stages which utilize a worm gear driving a ring gear to realize a 360:1 gear ratio. These are mounted concentrically with the rotation axes horizontal, allowing for utilization of a sample spinner/changer. Both stages incorporate Heidenhain optical encoders mounted so as to measure the angle of the ring gear to within $\pm 0.00028^\circ$ (1 arc second). The stages are driven by Oriental Motor 5 phase stepper motors that incorporated gear reducers of 10:1 for the θ stage and 5:1 for the 2θ , yielding steps sizes of 0.0002° (0.36 arc-seconds) and 0.0004° (0.72 arc-seconds) respectively. Visible in Figure 6 is the improved detector arm that has been balanced with respect to multiple rotation axes to minimize off-axis torque on the 2θ rotation stage.

Owing to the aforementioned criticality of both angle and distances in the divergent beam geometry, the concentricity of the rotation axes of the goniometer is of considerable interest. The manufacturer's specifications for the Huber 420 rotation stage claim an eccentricity of less than $3\ \mu\text{m}$, a wobble of less than 0.0008° (3 arc-seconds) and a transverse stiffness of $0.2\ \mu\text{rad/Nm}$. The construction of the goniometer assembly necessitated the development of a specialized jig to align the two 420 rotation stages with regards to both the concentricity (eccentricity) and parallelism (wobble) of their rotation axes. This is shown in Figure 7. Eccentricity was measured with an electronic finger gauge and steel ball to an uncertainty of $1\ \mu\text{m}$. Wobble was measured using an autocollimator that was quantifiably precise to 5 arc-seconds. The result was that overall eccentricity and wobble of the assembly met the specifications cited for the individual stages.

The optics, sample spinner, X-ray generator, and tube shield of the CDDBD were originally components of a Siemens D5000 diffractometer, ca. 1992. The optics are quite standard and include a variable divergence incident beam slit, graphite post-sample monochromator, anti-scatter slits, and a scintillation detector. The cable attached to the sample spinner which is visible in Figure 4, is a flexible drive for the spinner itself; the remote location of the drive motor isolates sample and machinery from the heat that the motor generates. The 2.2 kW copper tube of long fine focus geometry was operated at a power of 1.8 kW. This tube gives a source size of approximately 12 mm x 0.04 mm, while the goniometer radius is 217.5 mm. The variable divergence slit was set nominally to 0.8° for the collection of data discussed herein. A Soller slit with a divergence of 2.2° defined the axial divergence of the incident beam. A 2 mm anti-scatter slit was placed approximately 113 mm in front of the 0.2 mm (0.05°) receiving slit. The total path length of the scattered radiation, including the traverse through the monochromator, was ≈ 330 mm. The X-ray tube is mounted so as to provide adjustment of the source position vertically, the X-ray take-off angle, and parallelism between the line source and the goniometer rotation axis. The entire apparatus is mounted on an optical table within a temperature controlled laboratory space of $\pm 0.1^\circ$ C. Operation of the CDDBD was provided through control software written in LabVIEW. Data were recorded in true x-y format utilizing the angular measurements from the encoders.

The conditions required for diffractometer alignment are delineated and shown schematically in Figure 8. The first three of these requirements are established by construction of the instrument. Condition 4, that the X-ray source, sample surface, goniometer axes and detector slit be coplanar at the zero positions of both the θ and 2θ axes, requires a multi-step process to be met. First, the X-ray tube shield and divergence slit are aligned, using fluorescent screens to see the X-ray beam, to obtain the most basic condition that the beam, with a divergence of perhaps 1° , does indeed cross the rotation axes of the goniometer. The tube line source is then made parallel to the detector slit, and presumably to the rotational axis as well, with use of a $5\ \mu\text{m}$ pinhole mounted at the sample position. This serves to project an image of the source onto the detector slit. This experiment is performed absent the monochromator and with the width of the beam limited to 12 mm with additional shielding. The detector was then scanned through the beam as the tube tilt was adjusted sequentially to result in the data of Figure 9. One can see that parallelism is obtained with the setting that results in the narrowest peak of highest intensity.

The source, sample surface and detector slit were made coplanar using a glass tunnel (slit) shown schematically in Figure 10, mounted at the sample position. Preliminary scans were performed with the monochromator removed; once one has the approximate zero angles, it is re-installed. The nominal zero position of θ was determined by scanning the θ axis using an open detector. A 0.05 mm receiving slit was then inserted and 2θ scans were collected of the transmitted beam as the slit angle (θ) was sequentially incremented by 0.004° . Results are shown in Figure 11. One can observe the appearance and disappearance of the side lobes indicating the parallelism, or lack thereof, of the glass slit to the beam direction and hence θ and 2θ zero. At the zero angles determined with the data of Figure 11, the source, slit and detector are coplanar. However, it is by no means certain that the aforementioned plane bisects the goniometer rotation axes. The means to address this uncertainty consists of repeating the procedure with the theta stage inverted, i.e., driven to an angle of 180° . Once the zero angles of the second plane are determined, the true zero angles can be computed as $\frac{1}{2}$ the difference between those determined from the two experiments. With some trigonometry the Z height error of the sample stage is determined and a dial gauge can then be employed to adjust it. An iterative approach is then used to adjust the Z height until identical results at $\theta = 0^\circ$ and 180° (as per Figure 11) are realized with the peak centered on what is known to be the correct 2θ zero angle. A final $\theta/2\theta$ scan is taken with the glass slit to result in the data observed in

Figure 12. The centerline is the direct beam indicating the correct 2θ zero angle, while the symmetry of the two side lobes indicates that the θ stage is correctly zeroed.

Finally, the incident beam slit is adjusted so as to be centered as per condition 5 in Figure 8. The incident slit opening is set using the instrument control software by selecting a numerical value between 0 (closed) and about 350 (fully open). The actual divergence for any given value is measured by scanning the detector over the incident beam. It was found that the centerline of the beam changes slightly with the beam width; this is due to the fact that the slit blades themselves counter-rotate to adjust the opening rather than translate. The divergence slit setting is chosen to ensure that, at the lowest expected Bragg angle for the material of interest, the projected size of the beam on the sample is less than the 20 mm length of our sample holders. This consideration indicated an incident beam divergence of 0.8° for the SRMs of interest; a numerical value of 240 resulted in this level of divergence. With the slit opening set to this value, the slit assembly is then adjusted so that the slit is centered about $2\theta = 0$.

Qualification of the Diffractometer

SRMs 660a [12], consisting of LaB_6 , and 676a [13], consisting of alpha-alumina, were used for instrument characterization and validation [14], though SRM 1976a [15], a sintered alumina disc, would also be appropriate for this purpose. The analyses were conducted with two methods that accessed different aspects of instrument performance. The initial check involved consideration of data obtained from the fitting of individual profiles from a scan of SRM 660a. This approach permits a parametric analysis of instrument performance that is not constrained with respect to 2θ angle and serves primarily to test the performance of the goniometer. The second approach employs a Rietveld analysis wherein various models are functionally dependent on 2θ and used to verify the performance of the optics. SRM 660a, being the primary SRM for characterization of the IPF, is used to evaluate profile position and shape while 676a, being of lower symmetry, is suitable for evaluating the plausibility of parameters characterizing the instrument sensitivity such as Lorentz-Polarization and temperature factors.

Data from SRM 660a are fit with TOPAS using the split pseudo-Voigt profile shape function. This function typically yields the best fit of the aforementioned analytical profile shapes, to XRPD data. The FWHM, and their left and right values as a function of 2θ are shown in Figure 13 and 14. The continuous nature of the trends illustrated confirms that the goniometer assembly is functioning properly. At low angle, equatorial and axial divergence serves to asymmetrically broaden the profiles towards low 2θ angles; hence the upturn in FWHM of Figure 13 and the asymmetry illustrated in Figure 14. At high angles, dispersion effects predominate, leading to a $\tan\theta$ dependent increase in FWHM with 2θ . Also, both axial divergence and the asymmetry in the emission spectrum serve to asymmetrically broaden the profiles towards high angle. These effects are illustrated in Figures 13 and 14. The FWHM values approximating 0.065° in the 50° to 70° 2θ region are indicative of the ultimate resolution of the instrument; these are reasonable values given the selection of the various slits used in this configuration. The trends of Figures 13 and 14 are, therefore, consistent with expectations of the optical performance of the CDDBD. Rietveld analyses of data from SRM 660a and 676a resulted in refined physical parameters, instrumental, structural, and microstructural, that were verified to be within reasonable physical expectations.

The Application of the FPA Method

Data from SRM 660a were collected from selected regions corresponding to the 24 reflections accessible within the 2θ range of 20° to 150° . The scan parameters are given in Table 2. The angular widths of the ranges were chosen to include approximately 3 tenths of a degree of the apparent background straddling each profile. The step width was chosen to include at least eight

data points above the FWHM. The count time spent on each profile was inversely proportional to the observed diffraction intensity in order to result in a constant number of counts collected for each profile. The total data collection time was 40 hours. The extended time spent on the 222 peak is probably not warranted; it is exceedingly weak and located adjacent to other profiles. This is not so with the 400 line, however; it is relatively isolated and worth the extended time required.

The analysis via TOPAS discussed here was performed entirely in the GUI mode. As of the writing of this paper, “.inp” files are being developed that duplicate, and improve upon, the methods described herein and allow for their use with TOPAS Academic. They will be made available on the TOPAS wiki site [16]. While a full range of instrument parameters can be refined, those for which there exists a considerable level of certainty, such as 2θ zero and the divergent and receiving slit sizes, are typically left fixed. The Cu $K\alpha_1/K\alpha_2$ emission spectrum, as characterized by Hölzer, is shown in TOPAS “lam” format in Figure 15a. While one would never refine the $K\alpha_1$ position, it is the case that the graphite post monochromator affects the location and intensity of the $K\alpha_2$ profile relative to the $K\alpha_1$. The “lam” file of Figure 14a illustrates how these parameters are allowed to refine but with constraints applied to preserve the shape of $K\alpha_2$ profile as characterized by Hölzer. The use of models for Z height, in $\cos\theta$, and linear attenuation, in $\sin 2\theta$, of the sample are essential in the analysis of data from a divergent beam diffractometer. These parameters can have a large impact on the positions of profiles and are exceedingly difficult to determine with an explicit quantitative measurement. The background level was determined with the refinement of terms for a second order Chebyshev polynomial. The position and intensity of the “tube tails” were modeled with impulse or “top hat” functions. Three parameters were used to characterize this contribution: one for the intensity relative to the Cu $K\alpha_1$ line, and two for the positions on either side of each observed profile. The “full” axial divergence model [17, 18] was used to account for axial divergence. The optics of the instrument were consistent with “limiting case 2” of Table 1; the source, sample and receiving slit width were set nonetheless at 12, 18 and 15 mm. The incident optics used a 2.2° Soller slit while the receiving optics had none. However, given the 330 mm beam path length and 15 mm slit width, the axial divergence of the receiving optics was limited to 2.6° . The axial divergence was modeled by refining the primary and secondary Soller slit values constrained to be equality. Specimen broadening was modeled with a size broadening term, in $1/\cos\theta$, of a Lorentzian profile. Strain broadening terms invariably refined to zero and were not used in the work presented herein. The use of discrete files from each scan range precluded the refinement of structural parameters as the total counts represented in each file were not correlated to the “true” observed intensity of a given hkl, as per Table 2. Hence the analysis was not a true Rietveld structural refinement; however, all factors affecting profile shape and position were constrained with 2θ angle. A single lattice parameter was refined across all files.

In the course of the experiments associated with this work a close examination of the fits of individual profiles revealed a difficulty in the context of the profile breadth as a function of 2θ . The observation was investigated by allowing the Lorentzian broadening terms to refine independently; a trend appeared that was analogous to the dispersion effect. A considerable improvement in the quality of the fit was realized with a refinement of the Lorentzian breadths of the Cu emission spectrum. They were constrained as shown in Figure 15b to preserve asymmetric profile shape as modeled by Hölzer. One notes a 20 % reduction in the breadths determined through this study relative to those reported by Hölzer. The origin of this highly unexpected result is unclear, though it is thought that the graphite monochromator may be “clipping” the profiles, reducing the observed breadth. Further experiments are needed to explore this observation. The refinement of the breadths tended to reduce the stability of the analysis. Therefore, once the new breadths were determined, their refinement was discontinued with a new “lam” file that was written as per the constraints shown in the one of Figure 15a.

Typical results using the modified emission spectrum are shown in Figure 16. Fits of selected reflections are shown in Figures 18a-c. The global goodness-of-fit residual error parameter reached a value of 1.54. The quality of the fits is quite good. The refined parameters with a 2θ dependence are presented in Table 3. The axial divergence parameter defining the angular acceptance of the presumed Soller slits refines to 5.04° . This would appear to be in error given that a 2.2° Soller slit was in the incident beam; however, TOPAS reports the double angle of an axial divergence value. Thus a " 2.2° " Soller slit is reported as 4.4° in TOPAS. Thus, an angle estimate of 5.04° is not unreasonable. Attempts to improve on this approach with the axial divergence incident and receiving tied together proved fruitless resulting in higher residual error terms. The tube tail values are reasonable; care must be taken or they can refine to unrealistic values that generally connote a correlation with the $K\alpha_3$ component of the emission profile. Packing the sample to achieve high density invariably raised the reported value for attenuation by sample; however, it would also "raise" the reported Z height (negative Z moves the sample surface in the direction of the goniometer rotation axes). This is not a surprising observation. The refined Z height value is quite robust in its repeatability. This is not the case for the attenuation value, a fact reflected by its large reported estimated-standard-deviation.

The functionality of the FPA method can be considered in the context of the uniformity, or lack thereof, in the lattice parameter values from each hkl with respect to 2θ . To this end, the aforementioned "Rietveld" analysis was re-refined with several modifications. With the presumption that the profile shapes were appropriately fit, the objective was to determine how well the profile positions had been modeled. The principal parameters affecting profile shape, such as the axial divergence and crystallite size, were fixed at the "Rietveld" values. The sample attenuation and Z height were also fixed so that the corrections these models applied to the profile positions were preserved. The constraint previously applied to the lattice parameter was removed; a lattice parameter was computed for each hkl. Therefore, while the profile shapes remained largely unchanged, their positions were allowed to refine individually, with the corrections to line position previously determined with the "Rietveld" analysis being applied. The results are illustrated in Figure 17. The nature of these data has been duplicated, in essence, with the use of SRM 640d: the observations of Figure 16 are instrumental in origin. Below $40^\circ 2\theta$ there is a clear deviation; the sensitivity of lattice parameter with respect to 2θ is well known at low angle. A small shortcoming in the model can result in a large deviation, though a mechanism change in the sub $40^\circ 2\theta$ data is clearly indicated. Above $40^\circ 2\theta$, however, the deviation is notably small: $\pm 5 \times 10^{-6}$ nm. A clear trend in these data is apparent that calls for modeling. However; the error in profile position is nonetheless exceedingly small, on the order of $\pm 0.002^\circ 2\theta$. Consideration of the "Rietveld" vs. "profile" fits shown in Figure 18a-c demonstrate that the trend shown in Figure 17 is indicative of a most subtle effect on the profile positions.

Conclusions

The fundamental parameters approach was applied to data from a divergent beam X-ray powder diffractometer with an exceptionally stiff and accurate goniometer assembly and yielded excellent fits to the observations. Consistency in the lattice parameters determined from hkl reflections above $40^\circ 2\theta$ are consistent with a considerable improvement over generally accepted levels of uncertainty in lattice parameter measurements. While data indicate that slight refinements of the model applied to the FPA may be useful, the effects to be modeled are subtle indeed. The breadths of the Lorentzian profiles used to model the Cu $K\alpha$ emission spectrum, as reported by Hölzer, *et al.*, are on the order of 20 % in excess of those that provided the best fit to the data of the present work. We conjecture that this is an artifact of the graphite post monochromator.

References

- [1] H.M. Rietveld: Acta Cryst., Vol. 22, pp. 151-152 (1967)
- [2] H.M. Rietveld: J. Appl. Cryst., Vol. 2, pp. 65-71 (1969)
- [3] H.P. Klug, and L.E. Alexander: X-ray Diffraction Procedures, 2nd edition, John Wiley & Sons. (1974)
- [4] A.J.C. Wilson: Mathematical Theory of X-ray Powder Diffractometry, Gordon & Breach, New York (1963)
- [5] R.W. Cheary & A.A. Coelho: J. Appl. Cryst., Vol. 25, pp. 109-121 (1992).
- [6] R.W. Cheary & A.A. Coelho: Software: Xfit, Koalariet (1996) CCP14 Library, <http://wwwccp14.ac.uk>
- [7] TOPAS, General Profile and Structure Analysis Software for Powder Diffraction Data; V4.2, Bruker AXS GmbH, Karlsruhe, Germany
- [8] The International System of Units (SI). Bureau International des Poids et Mesures, Paris, 8th edition, 2006.
- [9] G. Hölzer, M. Fritsch, M. Deutsch, J. Härtwig, E. Förster: Phys. Rev. A, Vol. 56, Issue (6), (1997), pp. 4554-4568
- [10] M. Maskil, M. Deutsch: Phys. Rev. A, Vol. 38, (1988) pp. 3467-3472
- [11] J. Bergmann, R. Kleeberg, A. Haase, B. Breidenstein: In Proceedings of the 5th European Conference on Residual Stresses, edited by A.J. Böttger, R. Delhez, and E.J. Mittemeijer, Trans Tech Publications, 347-349, pp. 303-308 (2000)
- [12] SRM 660a; Lanthanum Hexaboride Powder Line Position and Line Shape Standard for Powder Diffraction; National Institute of Standards and Technology; U.S. Department of Commerce: Gaithersburg, MD (13 September 2000)
- [13] SRM 676a; Alumina Internal Standard for Quantitative Analysis by X-ray Powder Diffraction; National Institute of Standards and Technology; U.S. Department of Commerce: Gaithersburg, MD (28 January 2008)
- [14] J.P. Cline: in Industrial Applications of X-ray Diffraction, edited by F.H. Chung and D.K. Smith, pub. By Marcel Dekker, Inc, pp 903-917 (2000)
- [15] SRM 1976a; Instrument Response Standard for X-ray Powder Diffraction; National Institute of Standards and Technology; U.S. Department of Commerce: Gaithersburg, MD (10 April 2008)
- [16] See: <http://topas.dur.ac.uk/topaswiki/doku.php>
- [17] R.W. Cheary & A.A. Coelho: J. Appl. Cryst., Vol. 31, pp. 851-861 (1998)
- [18] R.W. Cheary & A.A. Coelho: J. Appl. Cryst., Vol. 31, pp. 862-868 (1998)

Acknowledgements

It is not the case that I could ever discuss the fundamental parameters approach without an acknowledgement of Bob Cheary. The community owes him great thanks for his work in this area.

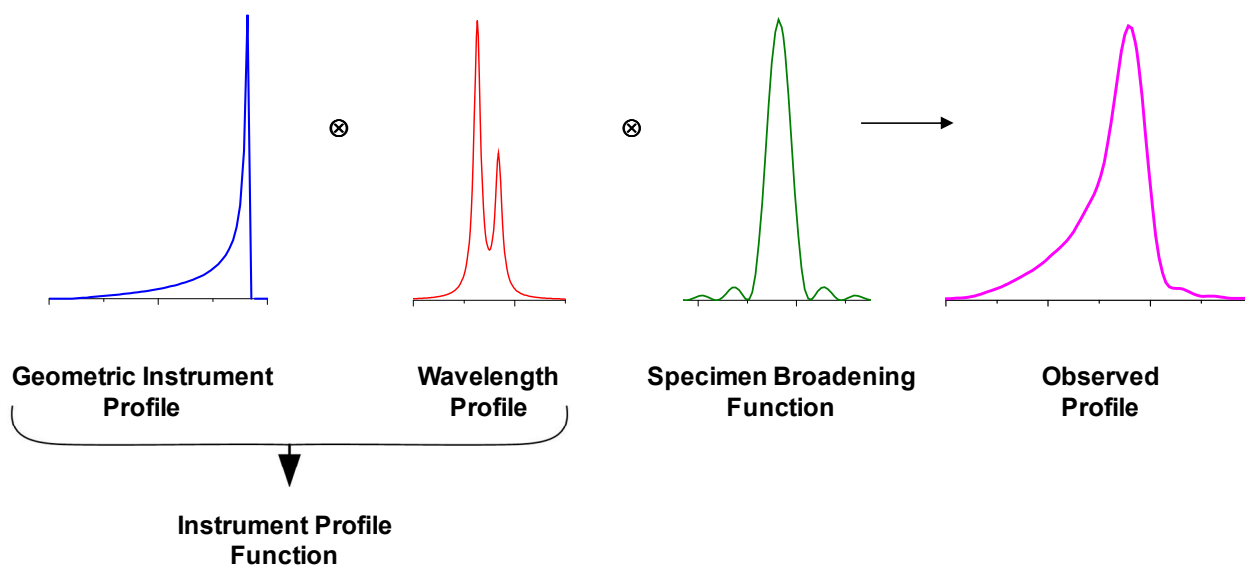


Figure 1. Diagrammatic representation of convolutions leading to the observed XRPD profile

Table 1. List of the aberrations comprising the geometric component of the IPF

ABERRATION	CONTROLLING PARAMETERS
Finite X-ray Source Width (w_x = source width)	Angle subtended by source = $\frac{w_x}{R}$
Finite Receiving Slit Width (w_r = receiving slit width)	Angle subtended by slit = $\frac{w_r}{R}$
Flat Specimen Error (Deviation of specimen surface from the focussing circle)	Angle of divergence slits = α (equatorial divergence)
(i) Axial Divergence – Limiting Case 1 No Soller slits in either the incident beam or diffracted beam	(i) Axial lengths of the, (a) x-ray source L_x (b) sample L_s (c) receiving slit L_r relative to the radius R of the diffractometer.
(ii) Axial Divergence – Limiting Case 2 Narrow Soller slits in both the incident beam and diffracted beam	(ii) Acceptance angles Δ_i and Δ_D of the incident beam and diffracted beam Soller slits, $\Delta = \frac{2h}{L_{\text{foil}}}$ where h = spacing of the foils and L_{foil} = length of foils
Specimen transparency (penetration of the beam under the specimen surface)	Penetration factor relative to diffractometer radius = $\frac{1}{\mu R}$
Specimen Displacement from the diffractometer axis	(a) Displacement of specimen T from axis (b) Amplitude δT of undulations on specimen surface

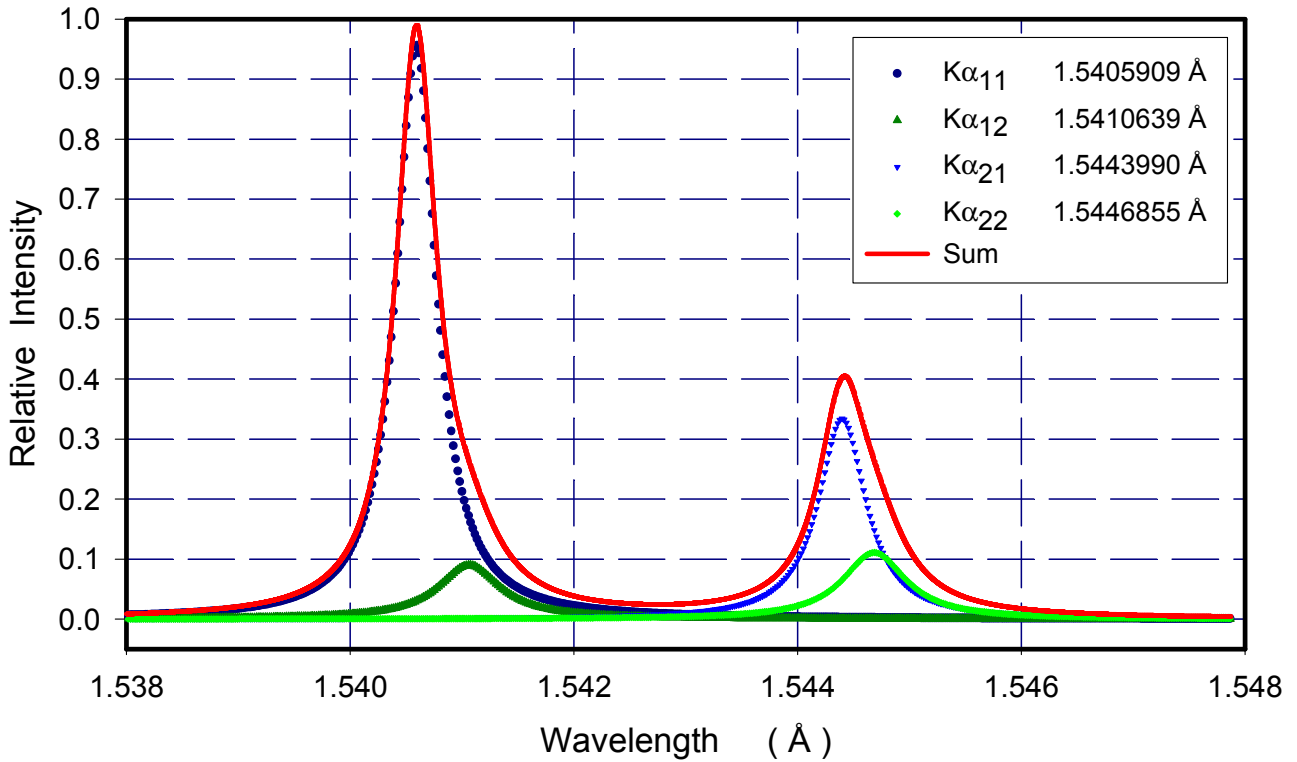


Figure 2. Emission spectrum of Cu $K\alpha$ radiation as characterized by Hölzer, *et al.* (1997)

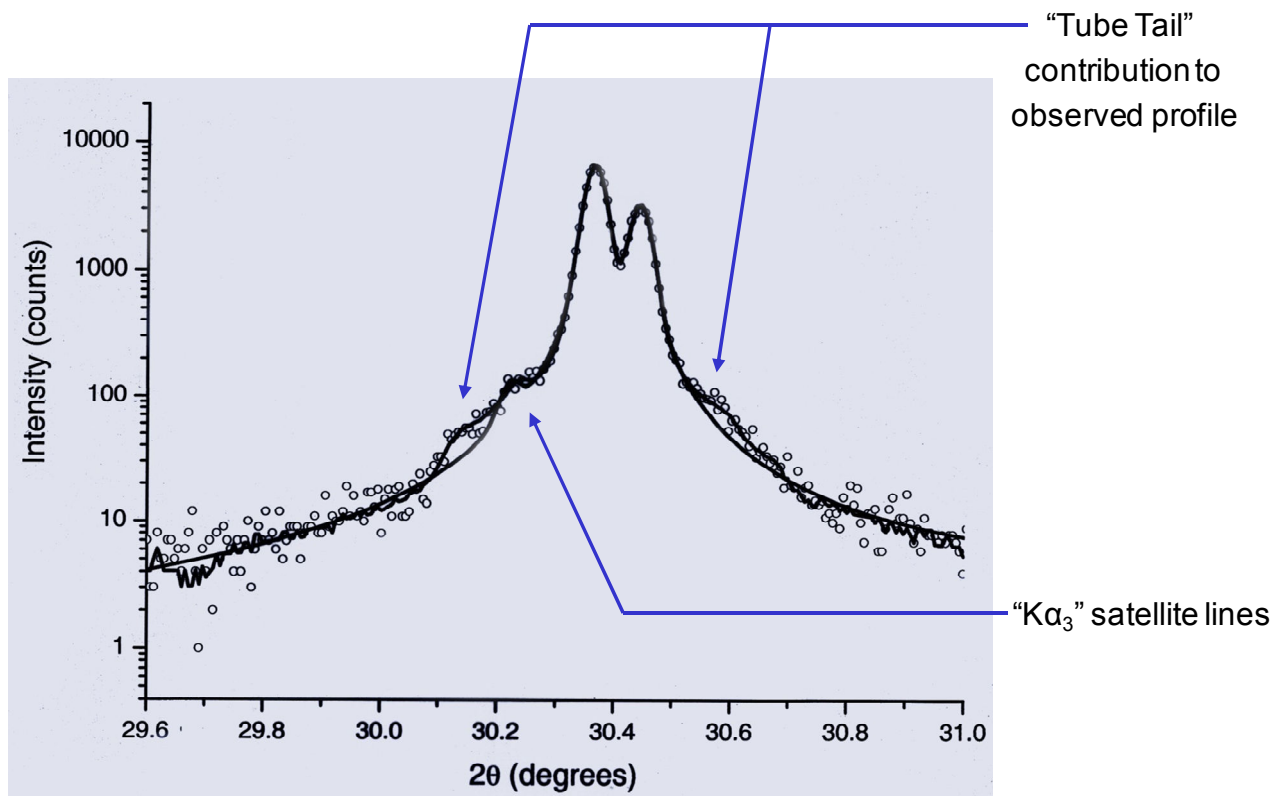


Figure 3. Illustration of the $K\alpha_3$ and “Tube Tails” contribution to an observed profile

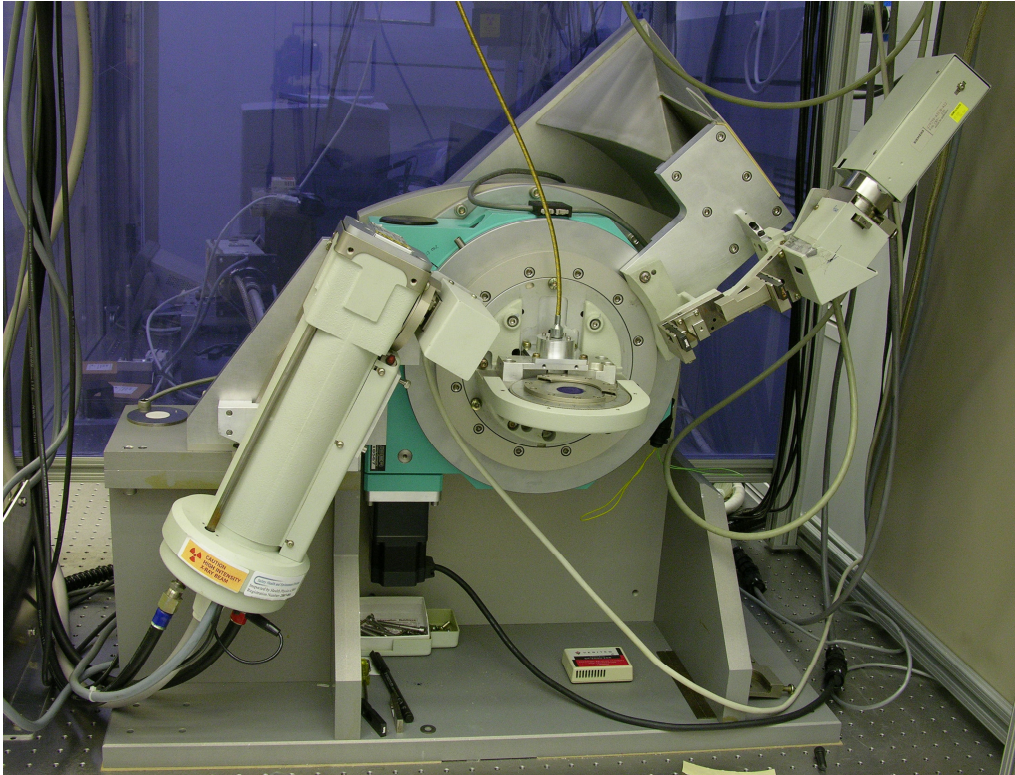


Figure 4. The front view of the CDDBD

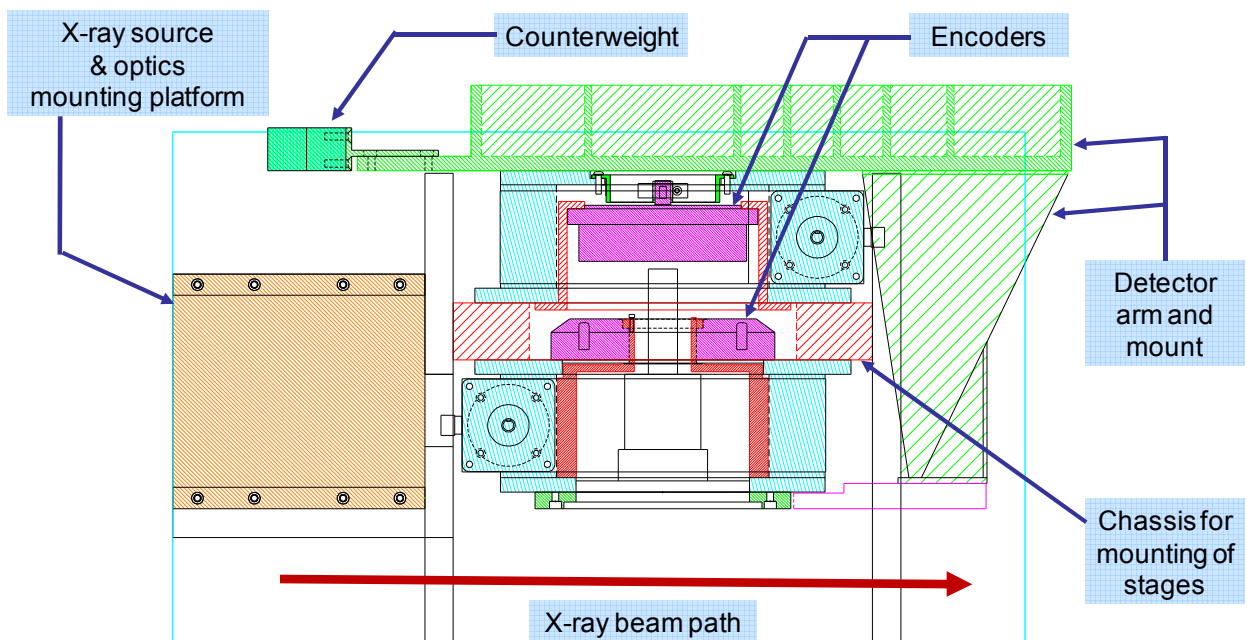


Figure 5. An over-head cutaway schematic diagram of the CDDBD

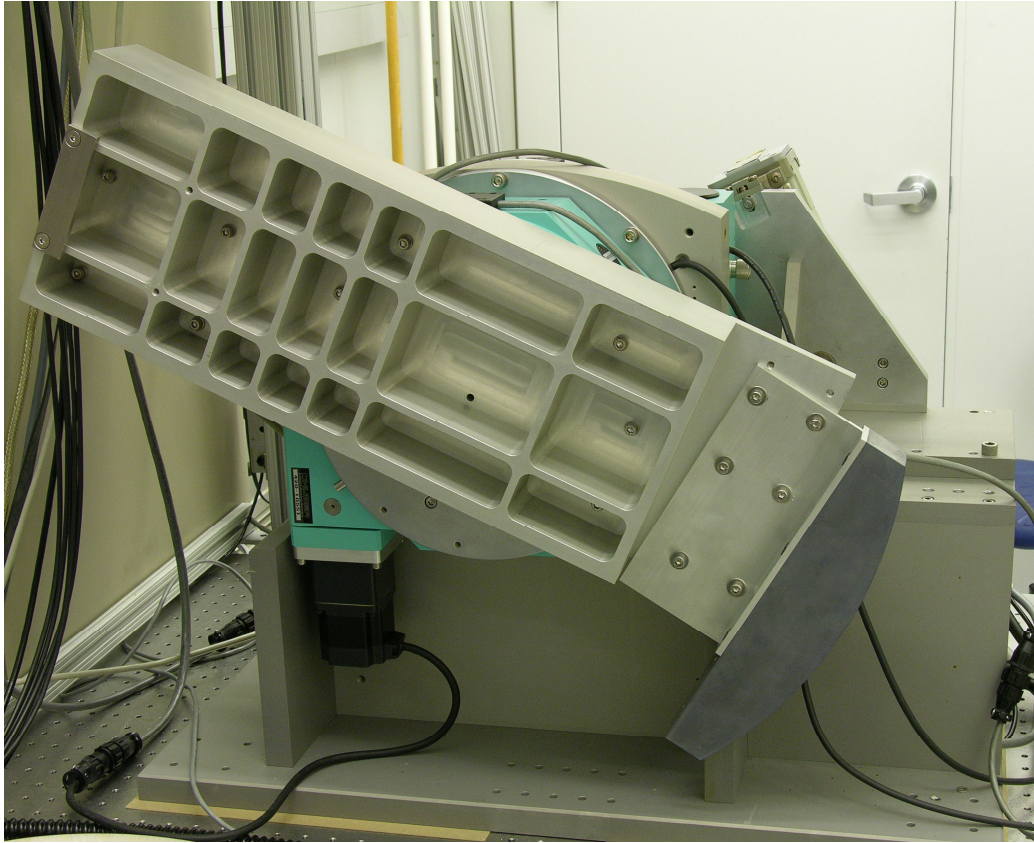
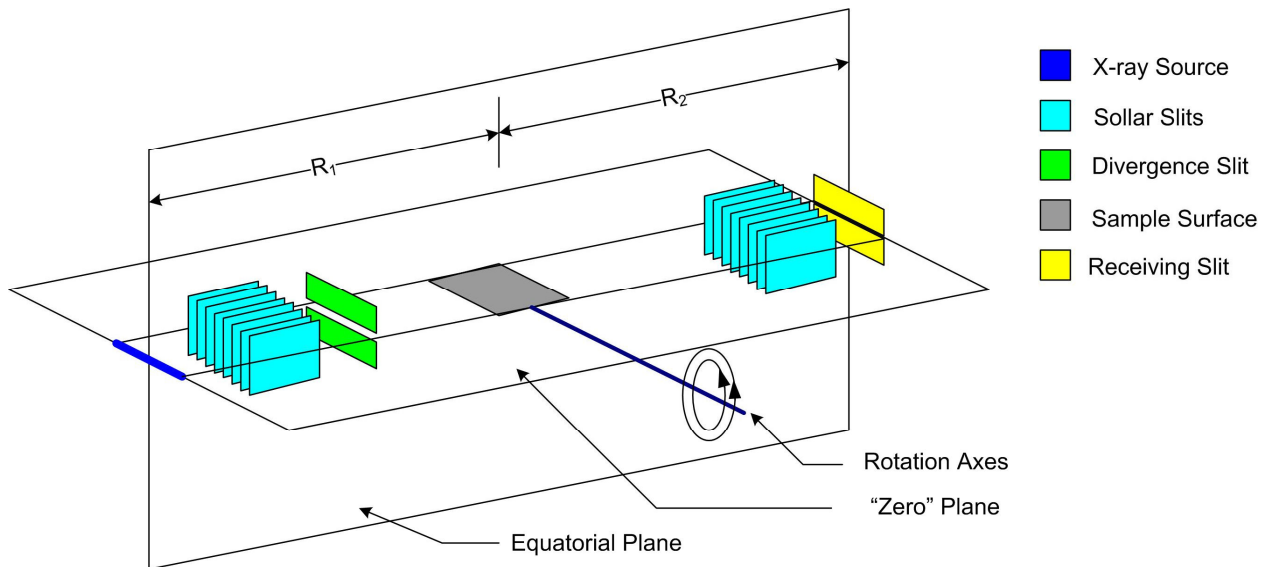


Figure 6. The stiff and balanced detector arm of the CDDBD



Figure 7. Albert Henins displaying his apparatus for aligning the rotation axes of the CDDBD



- 1) Source-to-sample distance equals sample-to-receiving slit distance ($R_1 = R_2$)
- 2) X-ray line source, sample, and receiving slit centered in plane of diffraction
- 3) Goniometer rotation axes are co-axial
- 4) X-ray line source, sample surface, detector slit, and goniometer rotation axes are co-planar, in the "zero" plane, at zero angle of theta and two-theta
- 5) Incident beam is centered on both equatorial and "zero" planes

Figure 8. Conditions fulfilled by a correctly aligned X-ray diffractometer

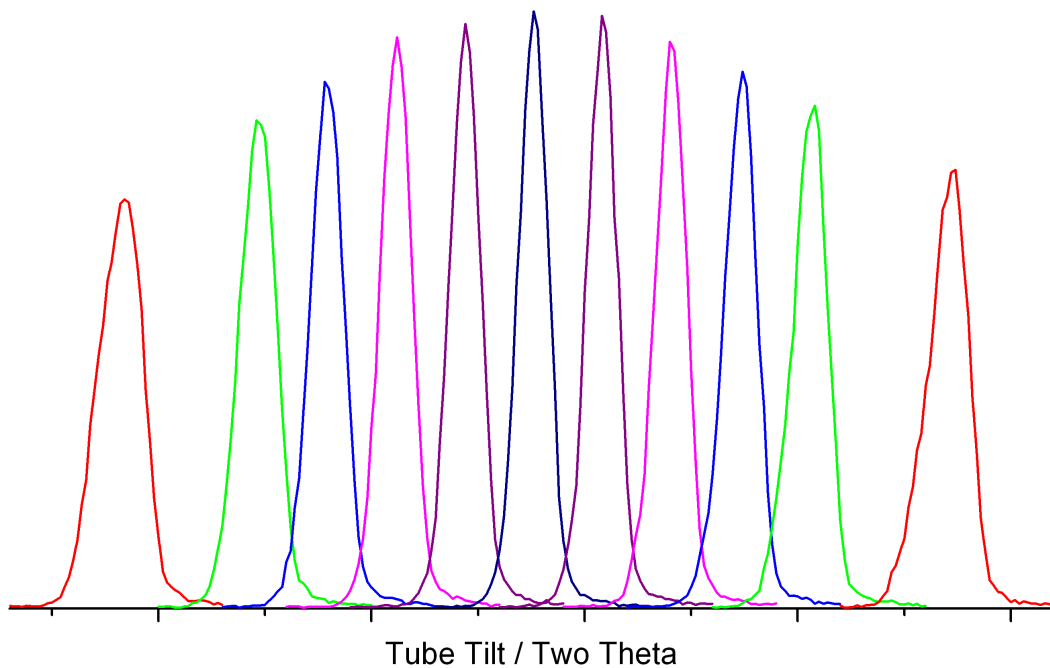


Figure 9. A sequence of 2θ scans, collected with the use of a pin hole, as a function of tube tilt

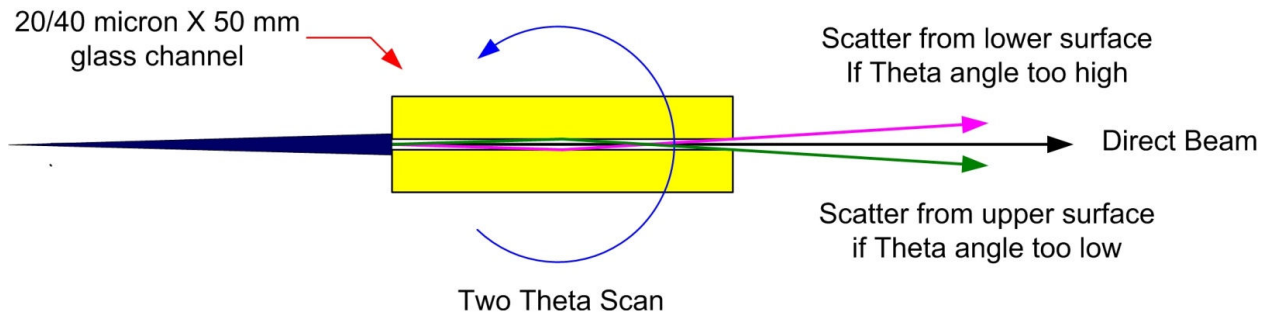


Figure 10. Diagrammatic illustration of the functionality of the glass tunnel/slit used for determination the θ and 2θ zero angles

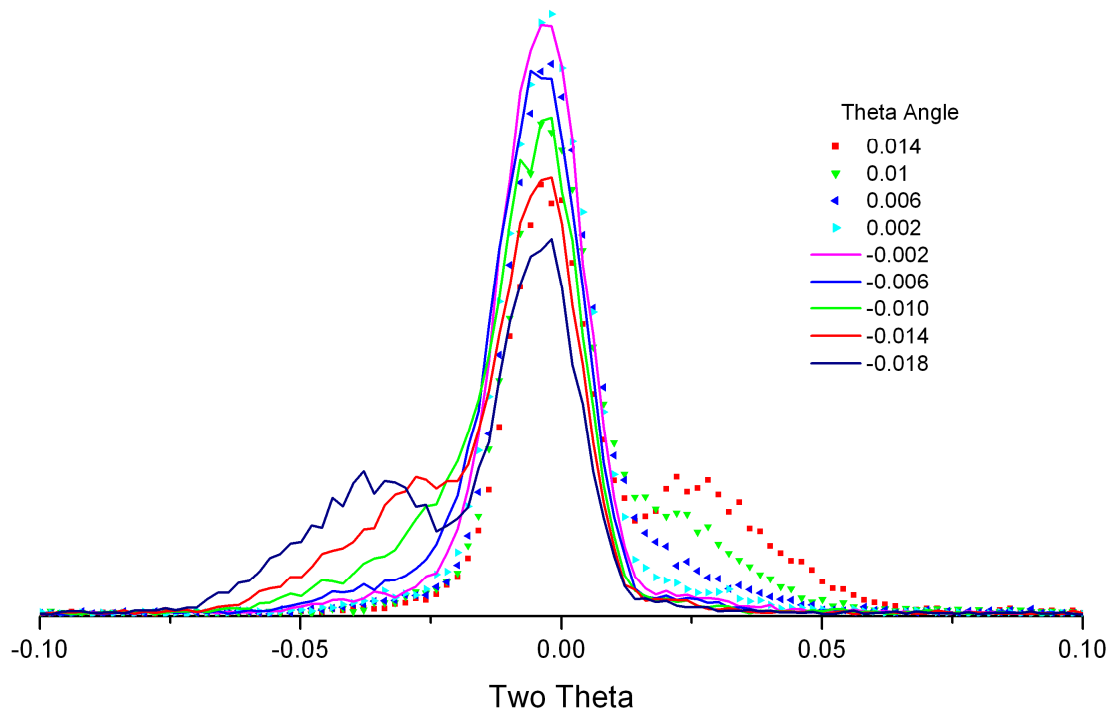


Figure 11. 2θ scans collected with the use of the glass tunnel/slit, as θ is incremented by 0.004° , used to determine the zero angles

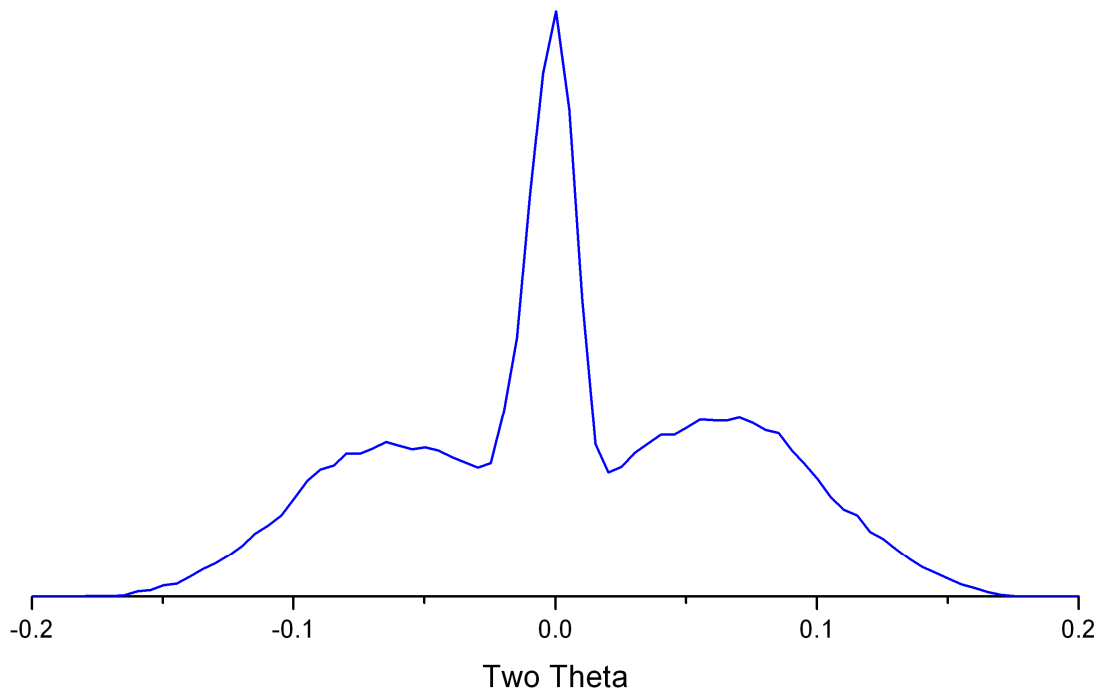


Figure 12. Final 2θ zero scan using the glass tunnel/slit indicating correct alignment

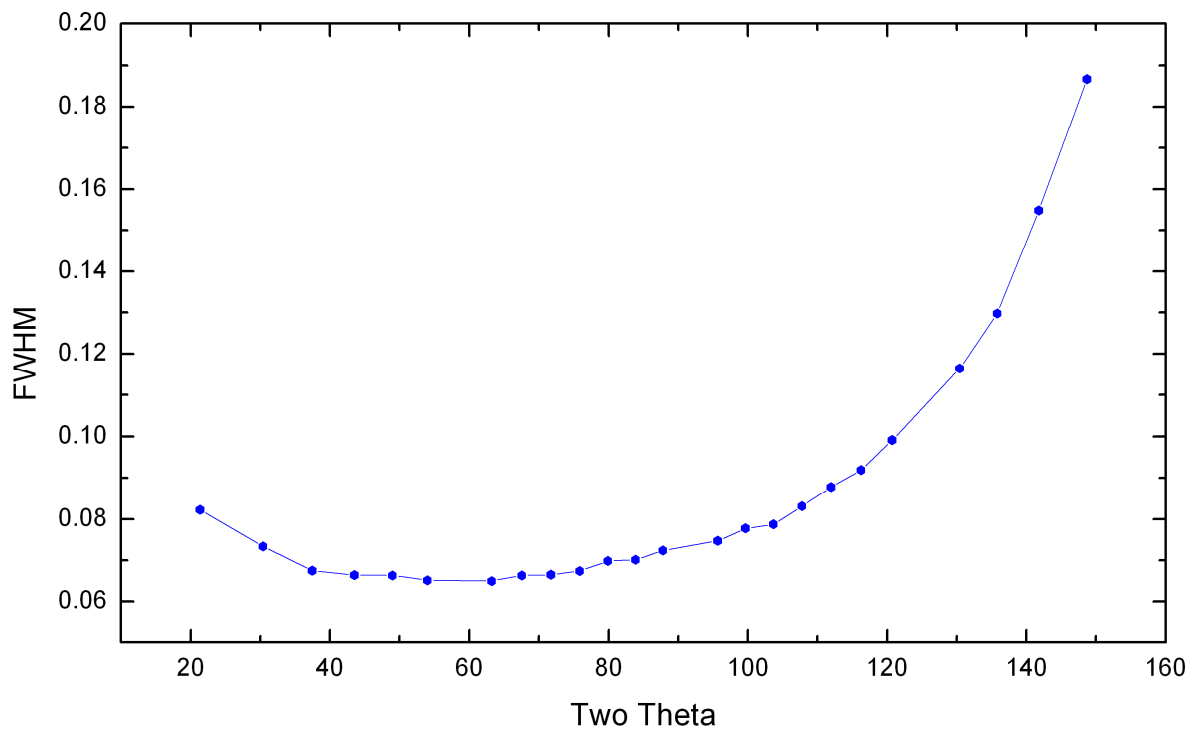


Figure 13. FWHM values determined from profile fitting of SRM 660a data as a function of 2θ angle

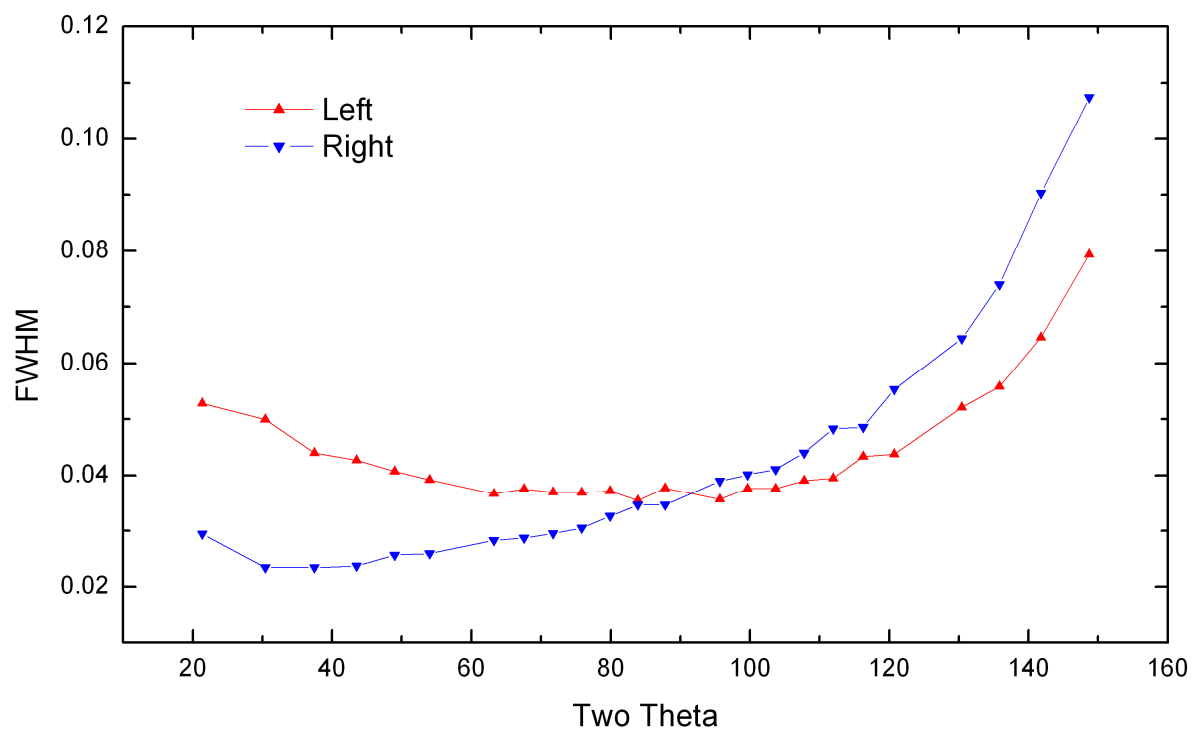


Figure 14. FWHM left and right values determined from profile fitting of SRM 660a data as a function of 2θ angle

Table 2. Run time parameters for collection of SRM 660a data for use in the FPA analysis

hkl	Start Angle	End Angle	Step Width (°)	Count Time (s)	Total Peak Time (min)
100	20.3	22.2	0.01	4	15.8
110	29.1	31.4	0.01	4	19.2
111	36.4	38.4	0.01	5	20.0
200	42.7	44.4	0.01	9	28.3
210	48	50	0.008	5	25.0
211	53.2	54.896	0.008	9	35.3
220	62.5	64.204	0.008	21	78.1
300	66.7	68.596	0.008	8	35.6
310	70.9	72.7	0.008	12	48.7
311	75	76.904	0.008	17	71.4
222	79.3	80.804	0.008	89	282.0
320	83	84.904	0.008	28	115.0
321	86.9	88.9	0.008	14	62.5
400	95	96.704	0.008	78	280.4
410	98.6	100.8	0.008	18	87.1
330	102.7	104.9	0.008	22	105.4
331	106.9	108.9	0.01	52	176.7
420	111.1	113.1	0.01	37	126.7
421	115.3	117.6	0.01	18	72.8
332	119.9	122.1	0.01	36	135.7
422	129.6	131.796	0.012	60	186.1
500	134.9	137.396	0.012	51	180.3
510	140.5	144	0.014	14	62.5
511	147.5	150.908	0.016	28	103.0
Total Time (hr)					40.0

a) Hölzer emission spectrum with refined $K\alpha_2$ position and intensity

lam

```
ymin_on_ymax 0.0001
la sat 0.0137 lo 1.534753 lh 3.6854
la 0.5711 lo 1.540591 lh 0.4374
la 0.0781 lo 1.541064 lh 0.6432
la la21 0.2328 lo l21 1.544433837 lh 0.5129
la =la21 .36; : 0.1039 lo =l21+.0003; : 1.544733837 lh 0.6872
```

b) Hölzer emission spectrum with refined breadth & $K\alpha_2$ position and intensity

lam

```
ymin_on_ymax 0.0001
la sat 0.01508366752 lo 1.534753 lh 3.6854
la 0.5711 lo 1.540591 lh lh11 0.3364
la 0.0781 lo 1.541064 lh =lh11 1.47; : 0.4945
la la21 0.2189657295 lo l21 1.544378604 lh lh21 0.3947
la =la21 .36; : 0.07882766262 lo =l21+.0003; : 1.544678604 lh =lh21 1.4; : 0.5526
```

Figure 15. TOPAS "lam" emission spectrum files: a) Hölzer, *et al.* (1997), b) This study

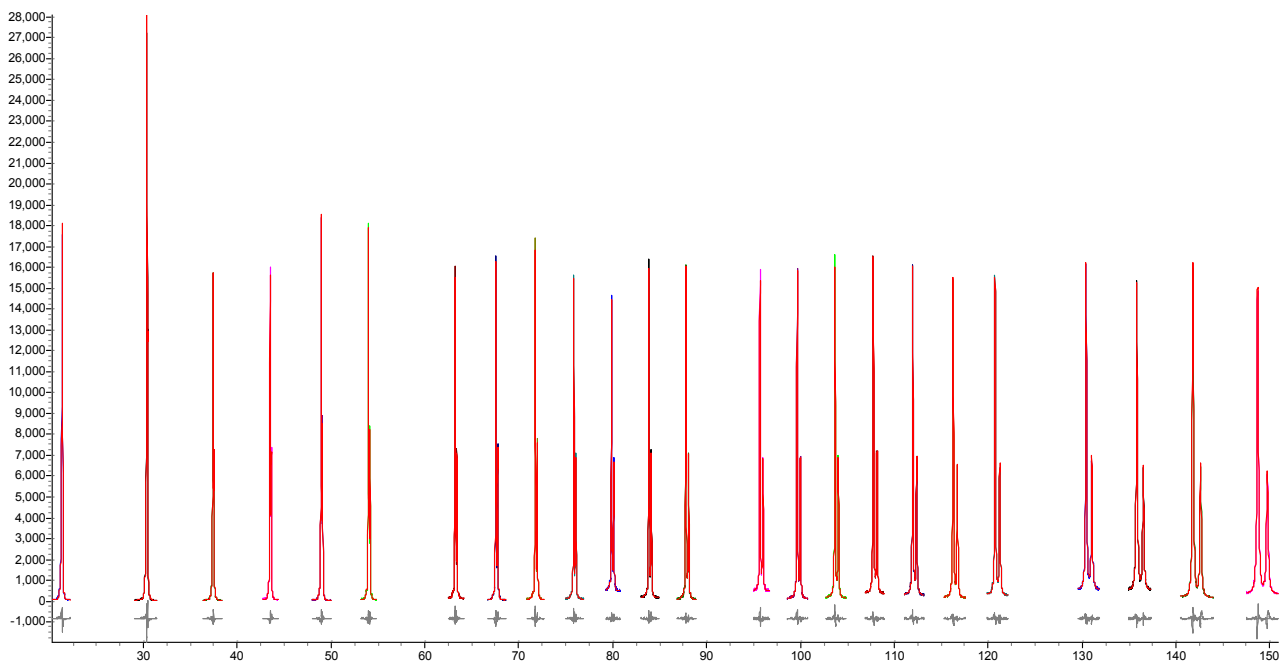


Figure 16. Results from "Rietveld" FPA analysis of SRM 660a data from the CDDBD

Table 3. Selected results from "Rietveld" analysis of SRM 660a

Instrument	
Primary radius (mm)	217.5
Secondary radius (mm)	217.5
Receiving slit width (mm)	0.2
FDS angle (°)	0.8
Full Axial Convolution	
Filament length (mm)	12
Sample length (mm)	18
Receiving Slit length (mm)	15
Primary Sollers (°)	5.037(11)
Secondary Sollers (°)	5.037(11)
Tube_Tails	
Source Width (mm)	0.04
Z1 (mm)	-0.9575(90)
Z2 (mm)	1.2719(75)
Fraction	0.00089(46)
Corrections	
Specimen displacement	-0.06371(29)
LP Factor	30
Absorption (1/cm)	1140(170)
Miscellaneous	
Convolution Steps	2
X Calculation Step	0.006
Structure 1	
Crystallite Size	
Cry size Lorentzian (nm)	927.6(82)
Lattice parameters	
a (Å)	4.1569461(24)

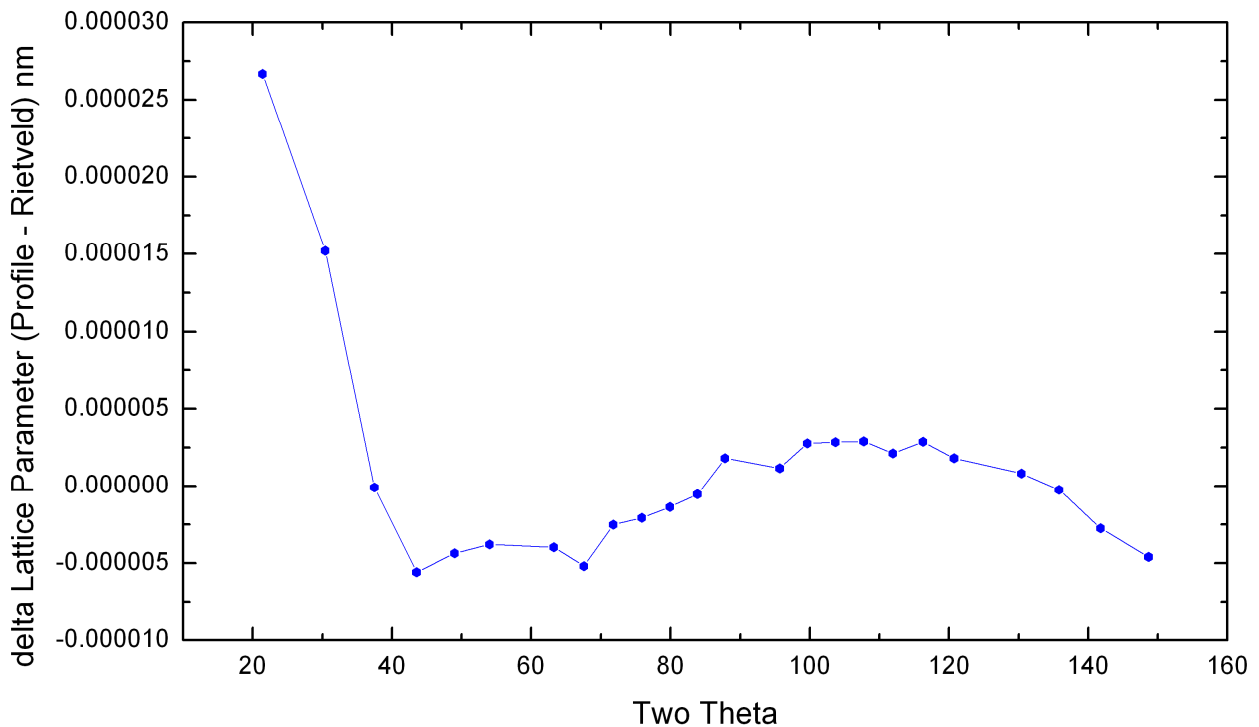
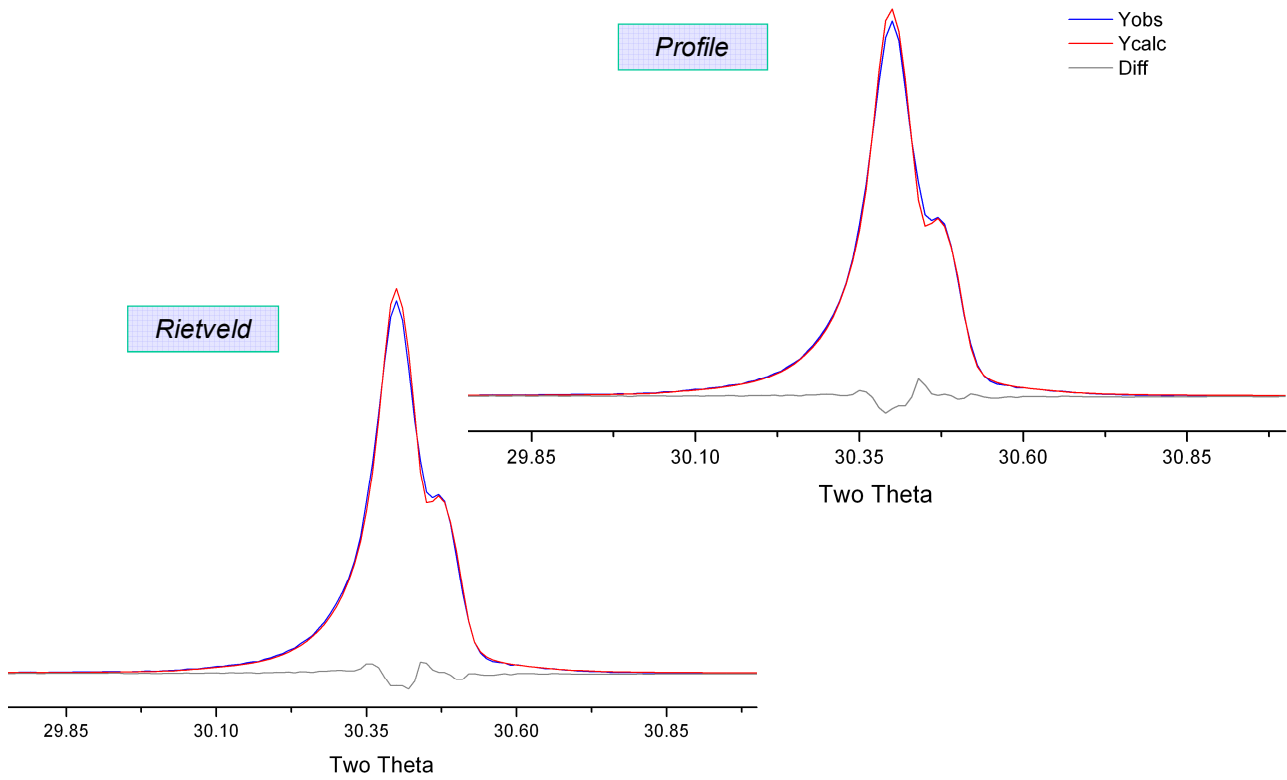
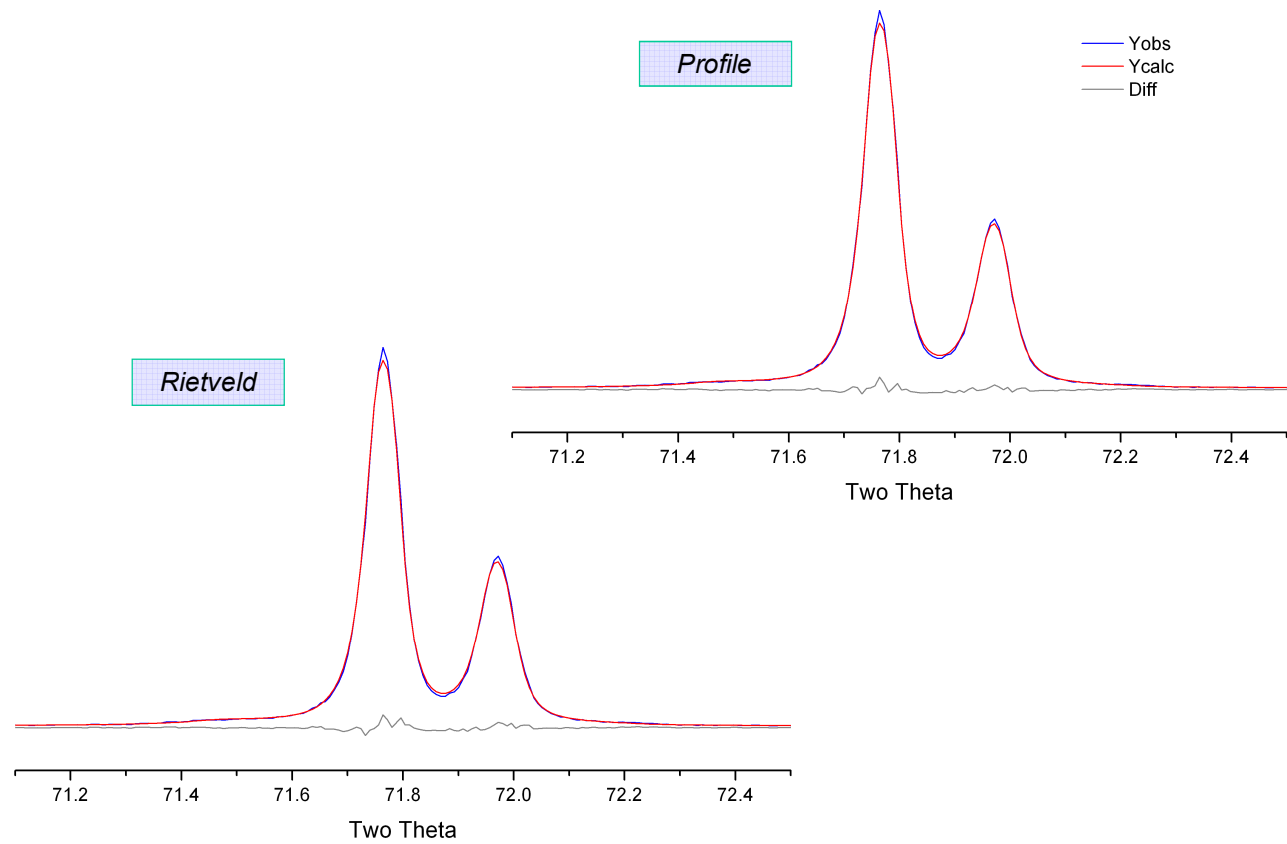


Figure 17. Difference curve for lattice parameter determined via "Rietveld" vs. "profile" analyses

Figure 18a. Fits to the LaB₆ 110 line, "Rietveld" and "Profile"Figure 18b. Fits to the LaB₆ 310 line, "Rietveld" and "Profile"

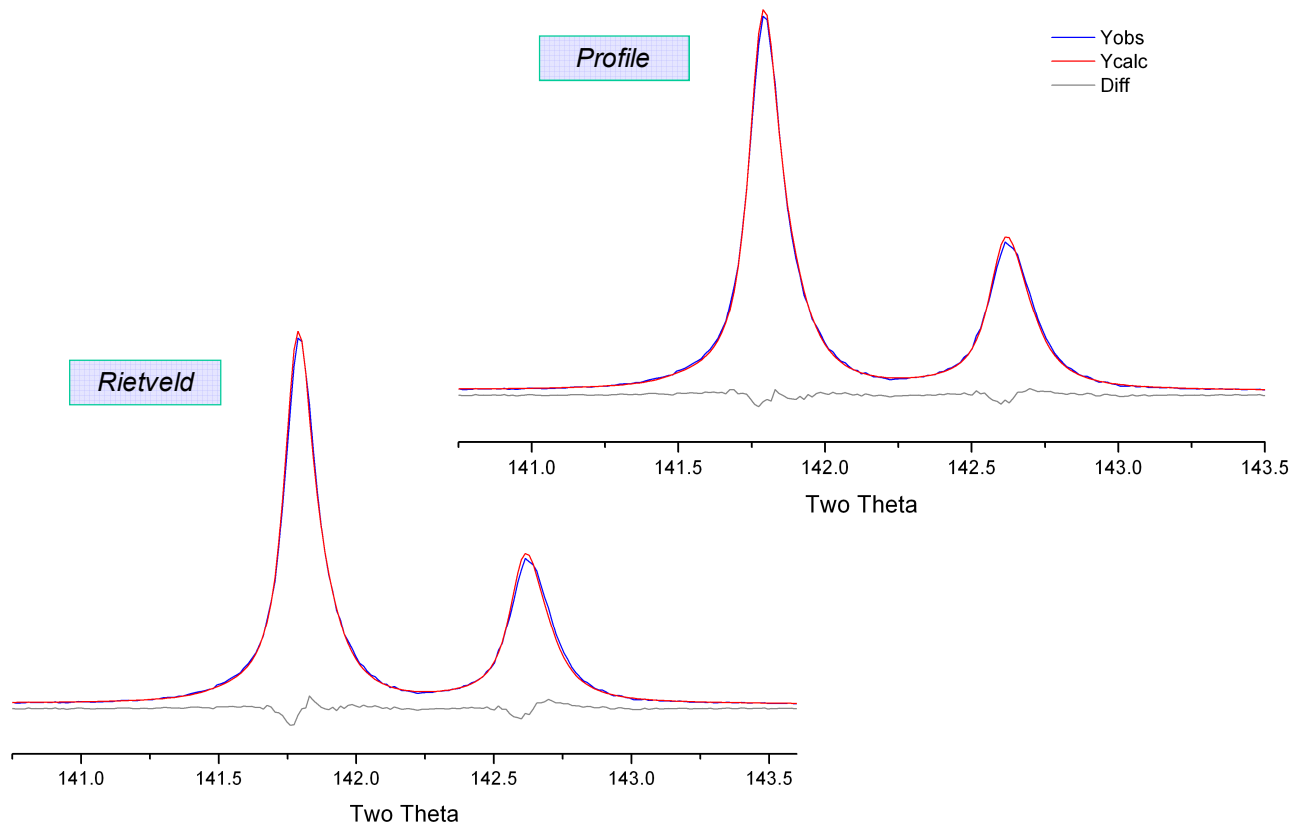


Figure 18c. Fits to the LaB₆ 510 line, "Rietveld" and "Profile"

Extending the Reach of Powder Diffraction Modelling

doi:10.4028/www.scientific.net/MSF.651

The Application of the Fundamental Parameters Approach as Implemented in TOPAS to Divergent Beam Powder Diffraction Data

doi:10.4028/www.scientific.net/MSF.651.201